

# Modifying La<sub>0.6</sub>Sr<sub>0.4</sub>MnO<sub>3</sub> Perovskites with Cr Incorporation for Fast Isothermal CO<sub>2</sub>-Splitting Kinetics in Solar-Driven Thermochemical Cycles

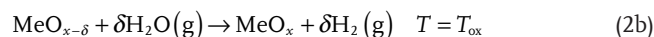
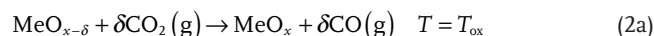
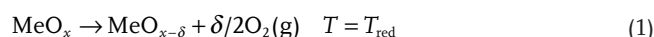
Alfonso J. Carrillo, Alexander H. Bork, Thierry Moser, Eva Sediva, Zachary D. Hood, and Jennifer L. M. Rupp\*

Perovskites are promising oxygen carriers for solar-driven thermochemical fuel production due to higher oxygen exchange capacity. Despite their higher fuel yield capacity, La<sub>0.6</sub>Sr<sub>0.4</sub>MnO<sub>3</sub> perovskite materials present slow CO<sub>2</sub>-splitting kinetics compared with state-of-the-art CeO<sub>2</sub>. In order to improve the CO production rates, the incorporation of Cr in La<sub>0.6</sub>Sr<sub>0.4</sub>MnO<sub>3</sub> is explored based on thermodynamic calculations that suggest an enhanced driving force toward CO<sub>2</sub> splitting at high temperatures for La<sub>0.6</sub>Sr<sub>0.4</sub>Cr<sub>x</sub>Mn<sub>1-x</sub>O<sub>3</sub> perovskites. Here, reported is a threefold faster CO fuel production for La<sub>0.6</sub>Sr<sub>0.4</sub>Cr<sub>0.85</sub>Mn<sub>0.15</sub>O<sub>3</sub> compared to conventional La<sub>0.6</sub>Sr<sub>0.4</sub>MnO<sub>3</sub>, and twofold faster than CeO<sub>2</sub> under isothermal redox cycling at 1400 °C, and high stability upon long-term cycling without any evidence of microstructural degradation. The findings suggest that with the proper design in terms of transition metal ion doping, it is possible to adjust perovskite compositions and reactor conditions for improved solar-to-fuel thermochemical production under nonconventional solar-driven thermochemical cycling schemes such as the here presented near isothermal operation.

## 1. Introduction

Solar fuels have emerged as a promising path for enabling the transition away from a fossil fuel based economy. Solar energy, the most abundant renewable source on Earth, can be transformed into fuels through several chemical routes.<sup>[1,2]</sup> The utilization of concentrated solar energy to drive thermochemical cycles of metal oxides represents an attractive way to produce solar fuels via a two-step process through which CO<sub>2</sub> and H<sub>2</sub>O can be transformed into renewable syngas.<sup>[3–5]</sup> In the first step of the process, concentrated solar energy is utilized to thermally reduce an oxide at high temperatures, creating oxygen vacancies, with the consequent release of lattice oxygen (Equation (1)). In the second step, conventionally operated at a lower temperature, the reduced form of the metal oxide uptakes oxygen from CO<sub>2</sub> and H<sub>2</sub>O injected in the solar reactor,

inducing splitting of the reactants by filling the oxygen vacancies of the oxide and producing CO and H<sub>2</sub>, commonly referred to as syngas (Equation (2a,b)).



In order to guarantee the efficiency of the process, the amount of oxygen released ( $\delta$ ) should be high, since it directly correlates with the amount of syngas produced in the second step. In addition, the oxide should show favorable thermodynamics toward splitting of CO<sub>2</sub> and H<sub>2</sub>O. Currently, the state-of-the-art material is ceria due to its suitable thermodynamic properties and fast kinetics for syngas production. Recently, ceria was reported to attain solar-to-fuel efficiencies as high as 5.25%.<sup>[6]</sup> Exploring alternative materials that provide a higher oxygen release and better splitting kinetics (when compared to that of ceria) is of scientific and technological interest.<sup>[7]</sup>

Dr. A. J. Carrillo,<sup>[†]</sup> Dr. A. H. Bork, T. Moser,<sup>[††]</sup> E. Sediva, Prof. J. L. M. Rupp  
Electrochemical Materials Group  
Department of Materials Science  
ETH Zurich  
Hönggerberggring 64, 8093 Zürich, Switzerland  
E-mail: jrupp@mit.edu

Dr. A. J. Carrillo, Dr. A. H. Bork, E. Sediva, Dr. Z. D. Hood, Prof. J. L. M. Rupp  
Electrochemical Materials Laboratory  
Department of Materials Science and Engineering  
Massachusetts Institute of Technology  
Cambridge, MA 02139, USA

Prof. J. L. M. Rupp  
Electrochemical Materials Laboratory  
Department of Electrical Engineering and Computer Science  
Massachusetts Institute of Technology  
Cambridge, MA 02139, USA

 The ORCID identification number(s) for the author(s) of this article can be found under <https://doi.org/10.1002/aenm.201803886>.

<sup>[†]</sup>Present address: Instituto de Tecnología Química (Universitat Politècnica de València-CSIC), Avda. Los Naranjos s/n, 46022 Valencia, Spain

<sup>[††]</sup>Present address: Laboratory for Thin Films and Photovoltaics, Empa-Swiss Federal Laboratories for Materials Science and Technology, Überlandstrasse 129, 8600 Dübendorf, Switzerland

DOI: 10.1002/aenm.201803886

In this respect, perovskite oxides ( $ABO_3$ ) have attracted much attention due to the plethora of different compositions that can be obtained by doping the A- and B-site cations to profit from their oxygen exchange, thermodynamics, and splitting kinetics in solar-to-fuel conversion, see a recent review in ref. [8]. Perovskites seem promising due to higher capacity for oxygen release than ceria, which eventually leads to higher CO and  $H_2$  yields. However, the favorable reduction comes at the cost of lower enthalpy and entropy values, which affect the solar-to-fuel efficiency<sup>[4,9]</sup> and  $CO_2$ -splitting kinetics.<sup>[10,11]</sup> High CO yields were obtained for  $La_{1-x}Sr_xMnO_3$  perovskites ( $x = 0.4$ ), but the decrease in enthalpy of reduction with increasing Sr content<sup>[12]</sup> also leads to a lower thermodynamic driving force for fuel production resulting in slower splitting kinetics.<sup>[10,11]</sup> Based on the amount of fuel produced per cycle, the  $La_{0.6}Sr_{0.4}MnO_3$  perovskite is still an attractive option for thermochemical syngas production.<sup>[10,11,13–20]</sup> provided the kinetics and/or thermodynamics are improved. This fact motivated the present work, in which we have explored the partial substitution of Mn by Cr with the purpose of studying its effect on the  $CO_2$ -splitting capabilities. This particular perovskite family, which has been focus of study as the anode in solid oxides fuel cells<sup>[21–23]</sup> and in methane conversion toward syngas,<sup>[24]</sup> has not been evaluated experimentally before for thermochemical solar-to-fuel production. Through very recent computation and thermodynamic equilibrium models based on CALPHAD, it was shown that the composition  $La_{0.6}Sr_{0.4}Mn_{0.2}Cr_{0.8}O_3$  exhibits a comparable solar-to-fuel efficiency of 2.7% when operated for isothermal splitting at 1500 °C to doped  $La_{0.6}Sr_{0.4}MnO_3$ , operated for cycling between 1500 °C and 1000 °C.<sup>[25]</sup> Motivated by this result, this work focuses on the synthesis, phase stability and performance of the solid solution series  $La_{0.6}Sr_{0.4}Mn_{1-x}Cr_xO_3$  for thermochemical solar-to-fuel conversion. The rationale behind the material choice is illustrated in the Ellingham diagram in **Figure 1**, based on data found in the literature.<sup>[26,27]</sup> From that thermodynamic data we can extract the Gibbs free energy of oxidation<sup>[28]</sup> of  $La_{0.6}Sr_{0.4}MnO_{3-\delta}$  and  $La_{0.6}Sr_{0.4}CrO_{3-\delta}$ ,  $\Delta g_{ox}$  for  $\delta = 0.1$ , and then calculate the Gibbs free energy for the  $CO_2$ -splitting reaction with  $La_{0.6}Sr_{0.4}MnO_{3-\delta}$  and  $La_{0.6}Sr_{0.4}CrO_{3-\delta}$  perovskites,  $\Delta g_{rxn}$  ( $\Delta g_{rxn} = \Delta g_{ox,\delta=0.1} + \Delta g_{CO_2}$ ; where  $\Delta g_{CO_2}$  is the Gibbs free energy for the  $CO_2$  splitting). Solid solutions of  $La_{0.6}Sr_{0.4}Cr_xMn_{1-x}O_3$  are expected to have thermodynamic properties,  $\Delta g_{rxn}$ , that lie in between the end members.<sup>[8,25,29]</sup> Based on this assumption the total Gibbs free energy of the oxidation of the perovskites  $La_{0.6}Sr_{0.4}Cr_xMn_{1-x}O_3$  by splitting  $CO_2$  will have a higher absolute value and higher thermodynamic driving force for CO production with a higher concentration of Cr, i.e., increasing values of  $x$ , compared to  $La_{0.6}Sr_{0.4}MnO_3$ . Importantly, at the working conditions relevant for thermochemical  $CO_2$  splitting,  $La_{0.6}Sr_{0.4}CrO_{3-\delta}$  perovskite shows very little oxygen release,<sup>[28]</sup> thus adjusting the Cr/Mn ratio in  $La_{0.6}Sr_{0.4}Cr_xMn_{1-x}O_3$  solid solutions would serve to optimize the tradeoff between oxygen release and enhanced thermodynamic driving force. In addition, under practical solar-to-fuel conditions, the kinetics of the oxidation in perovskites are governed by their thermodynamic properties rather than material kinetic properties as shown in our previous work on the perovskite  $La_{1-x}Sr_xMnO_3$ ,<sup>[11]</sup> and we expect that Cr doping will result in faster fuel production rates based on thermodynamic considerations depicted in Figure 1.

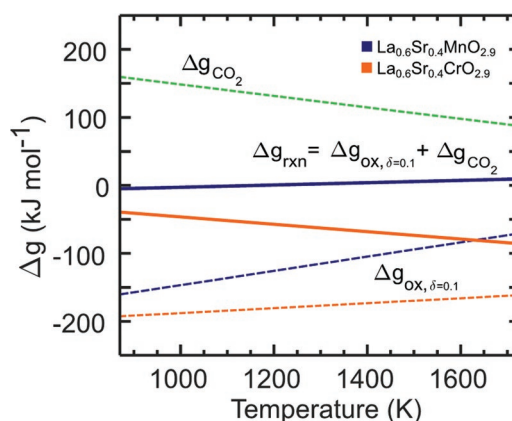


**Figure 1.** Thermodynamics for  $CO_2$  splitting of  $La_{0.6}Sr_{0.4}MnO_{3-\delta}$  (blue) and  $La_{0.6}Sr_{0.4}CrO_{3-\delta}$  (orange) perovskites, which serve as a rationale for testing the  $La_{0.6}Sr_{0.4}Cr_xMn_{1-x}O_{3-\delta}$  solid solutions. The green dashed line corresponds to the Gibbs energy change for the  $CO_2$ -splitting reaction ( $\Delta g_{CO_2}$ ), with temperature, data extracted from HSC Chemistry 6.1 from Outotec Research Oy. The dashed lines represent the Gibbs free energy change of oxidation by oxygen ( $\Delta g_{ox}$ ) for the perovskite at an oxygen nonstoichiometry of  $\delta = 0.1$ , calculated with data extracted from refs. [26,27]. The blue and orange solid lines represent the Gibbs free energy for the  $CO_2$ -splitting reaction with the  $La_{0.6}Sr_{0.4}MnO_{3-\delta}$  and  $La_{0.6}Sr_{0.4}CrO_{3-\delta}$  perovskites ( $\Delta g_{rxn}$ ), respectively. The properties of  $La_{0.6}Sr_{0.4}Cr_xMn_{1-x}O_{3-\delta}$  solid solutions are expected to lie in between the lines of the end-members.

Attending at the temperature range at which  $\Delta g_{rxn}$  shows more negative values, this would be especially relevant at high oxidation temperatures, indicating that those compositions would be promising materials for operation under isothermal cycling schemes ( $T_{red} = T_{ox}$ ).

Classically, thermochemical solar-to-fuel cycling is conducted in a two-step thermochemical cycle operating between a reduction and oxidation temperature as highlighted in Equations (1) and (2a,b). The reason for the two steps is that most applied materials such as  $La_{1-x}Sr_xMnO_3$  or  $CeO_2$  show optimal  $CO_2$ - and  $H_2O$ -splitting conditions at temperatures below 1000 °C, since the driving force for the splitting reaction,<sup>[11,12]</sup> i.e., a more negative  $\Delta g$ , increases when lowering the temperature (Figure 1). This driving force would be different for Cr-rich  $La_{0.6}Sr_{0.4}Cr_xMn_{1-x}O_3$ , since the Ellingham plot reveals a more negative  $\Delta g_{ox}$ , for  $La_{0.6}Sr_{0.4}CrO_3$  at higher temperatures<sup>[25]</sup> (1000–1400 °C) (Figure 1). This information indicates that Cr-rich  $La_{0.6}Sr_{0.4}Cr_xMn_{1-x}O_3$  might benefit from isothermal ( $T_{red} = T_{ox}$ ) or near-isothermal operation schemes. Isothermal thermochemical fuel production has been experimentally shown for the hercynite cycle in a stagnation flow reactor<sup>[30]</sup> and ceria,<sup>[31–33]</sup> the latter redox-material being tested with lab-scale membrane<sup>[31]</sup> and fixed-bed reactors.<sup>[32]</sup> Additionally, isothermal  $CO_2$  splitting has been performed with  $La_{1-x}Sr_xMnO_3$  and  $Y_{0.5}Sr_{0.5}MnO_3$  perovskites in thermobalance, the latter showing an enhanced fuel production at 1300 °C compared to  $La_{0.5}Sr_{0.5}MnO_3$ .<sup>[34]</sup> Operating isothermally or near-isothermally might benefit from faster kinetics and fewer thermal stresses in the material since temperature changes are not applied, resulting in higher morphological stability.<sup>[30,35]</sup> However,

to the best of our knowledge, the influence of temperature on the CO<sub>2</sub>- and/or H<sub>2</sub>O-splitting kinetics has not been evaluated at temperatures in the isothermal regime, and existent literature mainly covered kinetic aspects of CO<sub>2</sub>-and/or H<sub>2</sub>O-splitting reactions with Mn-based perovskite materials using temperature-swing two-step cycling.<sup>[10,17,36,37]</sup>

Erhart et al. carried out a process efficiency analysis pointing out that near-isothermal operation, e.g.,  $\Delta T = T_{\text{red}} - T_{\text{ox}} \approx 100\text{--}200\text{ }^\circ\text{C}$ , might be the most optimal scheme for materials with slow kinetics,<sup>[38]</sup> although the most optimum temperature interval for a given system would depend on the intrinsic thermodynamic and kinetic properties of each material. Furthermore, isothermal cycling shows several operational benefits, such as reduced downtime, since cooling down is avoided, and easier solid–solid heat recuperation can be established.<sup>[35]</sup>

In conclusion, thermodynamic considerations indicate that the new material candidate La<sub>0.6</sub>Sr<sub>0.4</sub>Cr<sub>x</sub>Mn<sub>1-x</sub>O<sub>3</sub> is supposed to benefit from operation in the near-isothermal to isothermal temperature range, but requires first experimental proof by synthesis and experimental validation of performance characteristics and stability for thermochemical solar-to-fuel conversion.

## 2. Results

### 2.1. Structural Characterization of La<sub>0.6</sub>Sr<sub>0.4</sub>Cr<sub>x</sub>Mn<sub>1-x</sub>O<sub>3</sub> Perovskite Materials

In this work, La<sub>0.6</sub>Sr<sub>0.4</sub>Cr<sub>x</sub>Mn<sub>1-x</sub>O<sub>3</sub> materials, with chromium concentrations of  $x = 0\text{--}0.85$  for the solid solution, were synthesized via the Pechini method. X-ray diffraction (XRD) patterns of the pristine samples showed that after calcination at 1400 °C for 24 h, all the materials, regardless of the Cr content, exhibited rhombohedral crystal structure (space group  $R\bar{3}c$ ) without the presence of any detectable phase segregation (Figure 2 and Table 1). Progressive Mn cation replacement by Cr on the transition metal ion perovskite site led to a shift of X-ray signatures to higher  $2\theta$  values as observed in the grey shadowed area around 47°, zoomed in Figure 1, indicating lattice shrinkage. To verify it and probe whether all synthesized materials reveal full solid solution mixing we determined the crystallographic cell volume evolution over the change in Cr-doping concentration (Figure 3a). All values of the lattice volume were obtained by Rietveld refinement, as exemplified for La<sub>0.6</sub>Sr<sub>0.4</sub>Cr<sub>0.3</sub>Mn<sub>0.7</sub>O<sub>3</sub> in Figure S1 in the Supporting Information. We report for up to 50% of chromium doping on the transition metal ion site ( $x = 0.5$ ), a linear decrease of the cell volume with increasing Cr content, in agreement with Vegard's law.<sup>[39]</sup> This result correlates well with a partial substitution of Mn<sup>3+</sup>,  $r_{\text{Mn}^{3+}} = 0.645\text{ \AA}$  in sixfold coordination, by Cr<sup>3+</sup> being of smaller ionic radius,  $r_{\text{Cr}^{3+}} = 0.615\text{ \AA}$ . For higher chromium concentrations a deviation from Vegard's law exists and

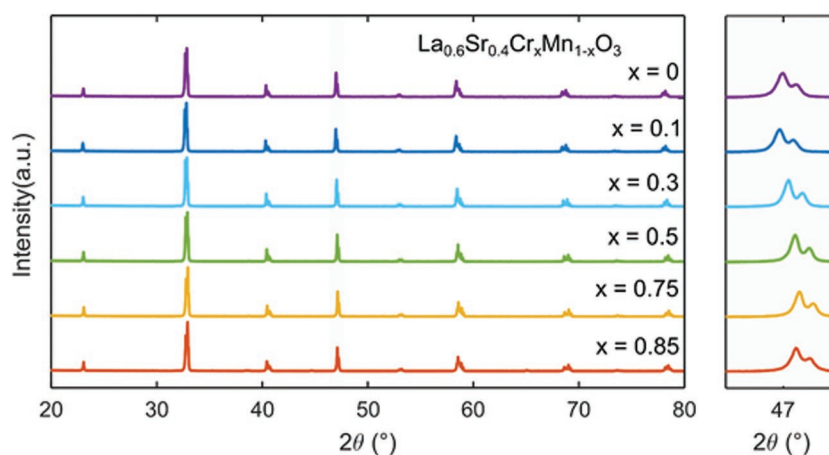


**Figure 2.** X-ray diffraction patterns of the as-synthesized La<sub>0.6</sub>Sr<sub>0.4</sub>Cr<sub>x</sub>Mn<sub>1-x</sub>O<sub>3</sub> materials. The  $2\theta$  range was zoomed out on the right panel in order to compare the shift of the reflection around  $2\theta = 47^\circ$  due to partial substitution of Mn cations by Cr cations.

cell volume stagnates at around  $344\text{ \AA}^3$ . The observation that Vegard's law is only followed up to an equal doping level of chromium and manganese for the perovskite, while keeping the same crystallographic phase might point to a potential valence change of the chromium, viz. partial substitution of Cr<sup>3+</sup> by Cr<sup>4+</sup> ( $r_{\text{Cr}^{4+}} = 0.55\text{ \AA}$ ,  $r_{\text{Cr}^{3+}} = 0.615\text{ \AA}$  in sixfold coordination).<sup>[40]</sup> Earlier studies on Sr and Ni-doped lanthanum chromates have pointed to an increased presence of Cr<sup>4+</sup> in temperature-programmed reduction (TPR) and X-ray photoelectron spectroscopy (XPS) measurements.<sup>[41]</sup>

To probe this hypothesis, we turn to Raman spectroscopy analyzing the near order structural characteristics of the perovskite solid solutions (Figure 3b). The Raman spectrum of the rhombohedral La<sub>0.6</sub>Sr<sub>0.4</sub>MnO<sub>3</sub> shows three broad peaks in the region between 400 and 700 cm<sup>-1</sup> (Figure 3b). Such modes have been observed in rhombohedral rare earth-doped manganites and were ascribed to the oxygen sublattice disorder<sup>[42]</sup> created by the incoherent Jahn–Teller distortions around Mn<sup>3+</sup> ( $d^4$ ). We measure that these Raman modes gradually develop into two sharper bands at 488 and 593 cm<sup>-1</sup> when adding Cr, which we ascribe to  $E_g$  modes of the rhombohedral LaCrO<sub>3</sub> according to Iliev et al.<sup>[43]</sup> The low-frequency mode around 200 cm<sup>-1</sup> we ascribe to the  $A_{1g}$  mode of the rhombohedral structure according to Dubroka et al.<sup>[44]</sup> When doping with

**Table 1.** Formula, lattice volume and average particle size of the La<sub>0.6</sub>Sr<sub>0.4</sub>Cr<sub>x</sub>Mn<sub>1-x</sub>O<sub>3</sub> materials.

Formula	Label	Lattice Volume [Å <sup>3</sup> ]	Avg. Particle size [μm]
La <sub>0.6</sub> Sr <sub>0.4</sub> MnO <sub>3</sub>	LSM	348.05	1.5 ± 0.5
La <sub>0.6</sub> Sr <sub>0.4</sub> Cr <sub>0.1</sub> Mn <sub>0.9</sub> O <sub>3</sub>	LSCM10	347.03	2.4 ± 0.8
La <sub>0.6</sub> Sr <sub>0.4</sub> Cr <sub>0.3</sub> Mn <sub>0.7</sub> O <sub>3</sub>	LSCM30	345.57	2.5 ± 0.7
La <sub>0.6</sub> Sr <sub>0.4</sub> Cr <sub>0.5</sub> Mn <sub>0.5</sub> O <sub>3</sub>	LSCM50	344.33	2.2 ± 0.7
La <sub>0.6</sub> Sr <sub>0.4</sub> Cr <sub>0.75</sub> Mn <sub>0.25</sub> O <sub>3</sub>	LSCM75	343.94	1.9 ± 0.5
La <sub>0.6</sub> Sr <sub>0.4</sub> Cr <sub>0.85</sub> Mn <sub>0.15</sub> O <sub>3</sub>	LSCM85	344.22	1.7 ± 0.6

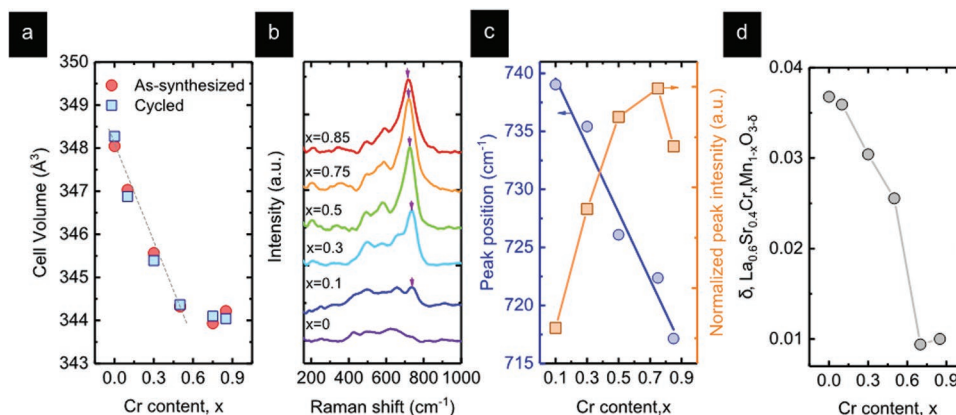


**Figure 3.** a) Cell volume values of La<sub>0.6</sub>Sr<sub>0.4</sub>Cr<sub>x</sub>Mn<sub>1-x</sub>O<sub>3</sub> perovskite materials with varying Cr concentration before and after cycling: XRD, cell volume parameters were obtained by Rietveld refinement. The grey-dashed line shows the linear regression between  $x = 0$  and  $x = 0.5$  compositional range that follows Vegard's law. b) Raman spectra of La<sub>0.6</sub>Sr<sub>0.4</sub>Cr<sub>x</sub>Mn<sub>1-x</sub>O<sub>3</sub> samples before cycling. Spectra were acquired at room temperature with a 532 nm laser. The arrows show the position of the band ascribed to A<sub>g</sub>-like mode. c) Plot showing the peak position of the band assigned to A<sub>g</sub>-like lattice vibration and its normalized intensity versus the Cr concentration,  $x$ , in La<sub>0.6</sub>Sr<sub>0.4</sub>Cr<sub>x</sub>Mn<sub>1-x</sub>O<sub>3</sub>. d) Oxygen nonstoichiometry for La<sub>0.6</sub>Sr<sub>0.4</sub>Cr<sub>x</sub>Mn<sub>1-x</sub>O<sub>3</sub> materials determined by thermogravimetric analyses. Perovskite powders were heated up to 1400 °C under Ar atmosphere.

10 mol% Cr,  $x = 0.1$ , a new band around 715 cm<sup>-1</sup> emerges, which grows and shifts to lower wavenumbers when increasing the Cr content (Figure 3c). The strong mode around 720 cm<sup>-1</sup> is in accordance with previously reported Raman spectra of La<sub>1-y</sub>Sr<sub>y</sub>Cr<sub>0.1</sub>Mn<sub>0.9</sub>O<sub>3</sub><sup>[44]</sup> and could be ascribed according to structurally related perovskite solid solutions<sup>[45–51]</sup> to an A<sub>g</sub>-like local oxygen breathing mode. Cr<sup>4+</sup> causes a Jahn–Teller distortion of the (Cr<sup>4+</sup>)-O<sub>6</sub> octahedron, which can create the local lattice distortion activating the 720 cm<sup>-1</sup> mode, see ref. [42] for details on the example of LaCrO<sub>3</sub>. However, the intensity of the mode (Figure 3c) follows the expected concentration of Cr<sup>3+</sup>, rising until  $x = 0.75$  as Cr<sup>3+</sup> replaces Mn<sup>3+</sup>. Interestingly, for  $x = 0.85$ , the relative peak intensity drops again to a lower value than for  $x = 0.75$  (48.15 and 57 a.u., respectively), indicating a lower presence of Cr<sup>4+</sup> in  $x = 0.85$  than in  $x = 0.75$ , which would correlate well with a slightly larger cell volume for  $x = 0.85$  (344.22 Å<sup>3</sup>) than  $x = 0.75$  (343.94 Å<sup>3</sup>). Although we cannot conclusively ascribe the mode at 715–740 cm<sup>-1</sup> to Cr<sup>4+</sup> or Cr<sup>3+</sup> based on these Raman observations and those reported in the literature, the correlation between the peak intensity of the A<sub>g</sub>-like mode and the Cr content can point to an increase of the Cr<sup>4+</sup>/Cr<sup>3+</sup> ratio with increasing Cr content for the La<sub>0.6</sub>Sr<sub>0.4</sub>Cr<sub>x</sub>Mn<sub>1-x</sub>O<sub>3</sub> materials. In addition, we confirmed the presence of Cr<sup>4+</sup> by XPS in the surface of La<sub>0.6</sub>Sr<sub>0.4</sub>Cr<sub>0.85</sub>Mn<sub>0.15</sub>O<sub>3</sub> before and after a thermochemical durability cycle. These results are discussed in detail in Section 2.3.

Collectively, we conclude that for doping up to  $x = 0.5$  a full solid solution prevails in the material. Doping beyond  $x = 0.75$  the Cr concentration maintains the rhombohedral structure, however, XRD and Raman analysis of the A<sub>g</sub>-like mode point to a progressing Jahn–Teller distortion and change in the chromium valence change with a higher Cr<sup>4+</sup> concentration.

Figure 3d displays the oxygen release,  $\delta$ , during reduction under Ar up to 1400 °C of the perovskite powders in a thermogravimetric analyzer. Introducing more Cr dopants on the transition metal ion position of the manganese results in a generally lowered oxygen release. For example, it reduces from  $\delta \approx 0.037$  at  $x = 0$  to  $\delta \approx 0.01$  for  $x = 0.75–0.85$  (Figure 3d); this result would also imply

a lower fuel production capacity for the water or CO<sub>2</sub>-splitting step (Equation (2a)). The lowered oxygen exchange with increasing Cr content in La<sub>0.6</sub>Sr<sub>0.4</sub>Cr<sub>x</sub>Mn<sub>1-x</sub>O<sub>3</sub> agrees well with thermodynamic data in the literature, indicating that lanthanum chromates require stronger reducing conditions to release oxygen.<sup>[8]</sup> The lower oxygen release is ascribed to the higher presence of less reducible Cr<sup>4+</sup> cations, in agreement with the XRD and Raman observations.

The influence of Cr-doping on the microstructure was studied by scanning electron microscope (SEM) (Figure 4). It was observed that incorporation of chromium, as low as  $x = 0.1$ , induced particle growth compared to pure La<sub>0.6</sub>Sr<sub>0.4</sub>MnO<sub>3</sub>. The average grain size increases from 1.5 ± 0.5 to 2.5 ± 0.7 μm, for increase of chromium to  $x = 0.3$  (Figure 4b and Table 1). Similar behavior was found in literature for (Sr<sub>0.7</sub>Ce<sub>0.3</sub>)<sub>1-x</sub>Mn<sub>1-y</sub>Cr<sub>y</sub>O<sub>3-δ</sub>, where authors reported grain sizes of 1–4 μm for  $y = 0$  to 7–14 μm for  $y = 0.5$ .<sup>[52]</sup> Additionally Saravanan et al. observed an increase in grain growth with an increase in Cr content on (La<sub>0.8</sub>Ca<sub>0.2</sub>)(Cr<sub>0.9-x</sub>Co<sub>0.1</sub>Mn<sub>x</sub>)O<sub>3</sub> perovskites, viz. 0.666 μm for  $x = 0.03$  and 0.351 μm for  $x = 0.12$ .<sup>[53]</sup> In these reports, the authors ascribed the particle growth to Cr incorporation. One possible explanation can be related with the presence of Cr that during the high-temperature processing can form volatile species such as CrO<sub>3</sub> that then are deposited again on the surface of the perovskite phase forming SrCrO<sub>4</sub> nuclei, which act as nucleation sites for the eventual perovskite particle growth.<sup>[54,55]</sup> Interestingly, when increasing the Cr content up to  $x = 0.85$  (Figure 3f) average grain size decrease by 30% to 1.7 ± 0.6 μm. Notably this decrease in grain size is accompanied by a slightly higher presence of intergranular pores and also a higher degree of grain faceting is exhibited (Figure 4f). Through the following, we test the compositions of La<sub>0.6</sub>Sr<sub>0.4</sub>Cr<sub>x</sub>Mn<sub>1-x</sub>O<sub>3</sub> for thermochemical cycling and also comment on the microstructure evolution during testing.

## 2.2. Thermochemical Fuel Production and CO<sub>2</sub>-Splitting Kinetics

After identifying the implications of Cr-incorporation on the physicochemical properties of these perovskites, we turn to

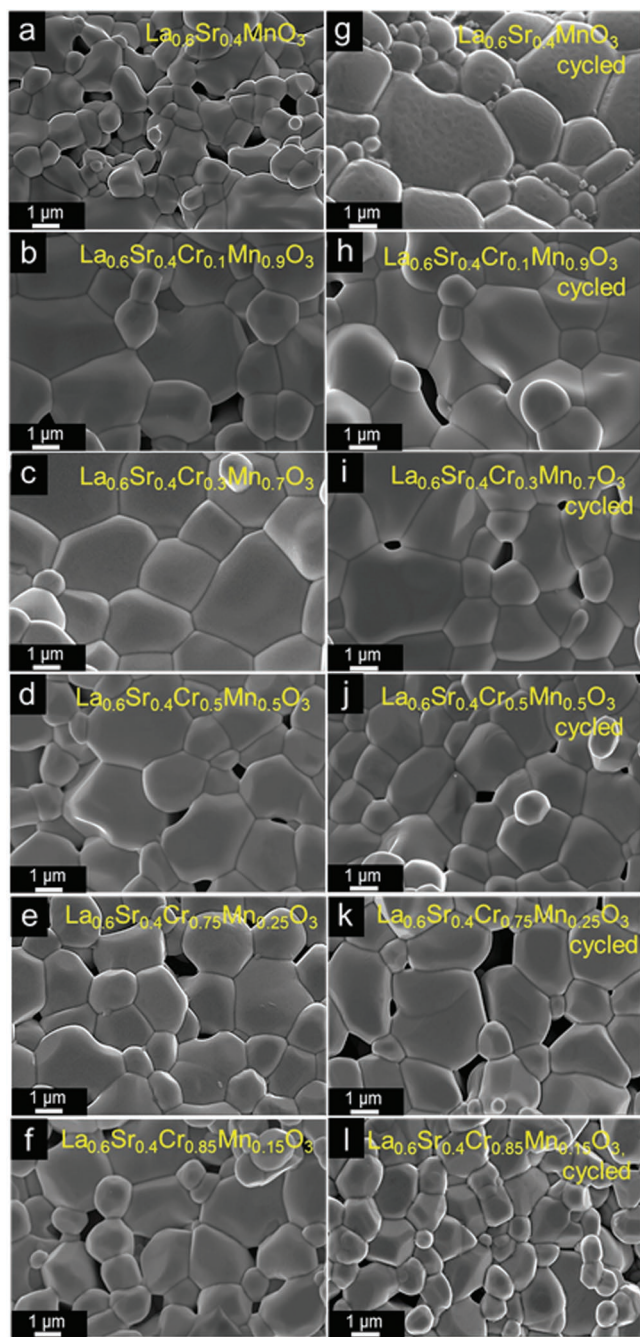


**Figure 4.** SEM micrographs of a–f) as-synthesized and g–l) cycled  $\text{La}_{0.6}\text{Sr}_{0.4}\text{Cr}_x\text{Mn}_{1-x}\text{O}_3$  powders. a)  $x = 0$ , b)  $x = 0.1$ , c)  $x = 0.3$ , d)  $x = 0.5$ , e)  $x = 0.75$ , and f)  $x = 0.85$ .

the investigation of the fuel production performance. Through this study, we evaluated thermochemical splitting cycles for  $\text{La}_{0.6}\text{Sr}_{0.4}\text{Cr}_x\text{Mn}_{1-x}\text{O}_3$  at both near-isothermal and isothermal conditions, for which we exemplify on the splitting of  $\text{CO}_2$ , tested in a high-temperature fixed bed reactor, see the Experimental Section for more details. Importantly, we will compare the rate production and CO yields with two of the state-of-the-art materials, the perovskite  $\text{La}_{0.6}\text{Sr}_{0.4}\text{MnO}_3$  and  $\text{CeO}_2$ .

Thermochemical cycling tests were performed to the  $\text{La}_{0.6}\text{Sr}_{0.4}\text{Cr}_x\text{Mn}_{1-x}\text{O}_3$  materials from  $x = 0$  to  $x = 0.85$ , in which  $\text{O}_2$  release and CO production were monitored for eight consecutive cycles, evaluating the influence of the reduction (1200, 1300, and 1400 °C) and oxidation temperatures (1000–1400 °C) (Figure S2, Supporting Information), showing that for every temperature and cycle tested, all the  $\text{La}_{0.6}\text{Sr}_{0.4}\text{Cr}_x\text{Mn}_{1-x}\text{O}_3$  perovskite materials exhibited  $\text{O}_2$  and CO production in the reduction/oxidation cycles, respectively. The results obtained during the first three isothermal cycles reflect that performing reduction at higher temperatures leads to higher  $\text{O}_2$  release and, thus, higher CO production for every sample, indicating that 1400 °C is the most suitable temperature for isothermal cycling for this family of perovskites. For each material, the temperature increase leads also to faster CO production rate. For instance, for  $\text{La}_{0.6}\text{Sr}_{0.4}\text{Cr}_{0.3}\text{Mn}_{0.7}\text{O}_3$ , the CO peak rate increases from  $0.17 \text{ mL min}^{-1} \text{ g}^{-1}$  at 1200 °C to  $1.14 \text{ mL min}^{-1} \text{ g}^{-1}$  at 1400 °C.

Interestingly, we observed that isothermal  $\text{CO}_2$  splitting, especially at 1300 and 1400 °C, generates concomitantly  $\text{O}_2$ . The source of  $\text{O}_2$  production during  $\text{CO}_2$  splitting is ascribed to the thermolysis of  $\text{CO}_2$  ( $\text{CO}_2 \rightarrow \text{CO} + 1/2\text{O}_2$ ), mainly catalyzed by the alumina reactor inner surface and the powder bed at high temperatures (Figure S3, Supporting Information). This effect has been reported for isothermal  $\text{H}_2$  and CO production with ceria<sup>[31,33]</sup> and hercynite,<sup>[56]</sup> however, this is the first observation of this kind for isothermal cycling of perovskites, since previous studies rely on thermogravimetric analysis (TGA)<sup>[34,57]</sup> that cannot monitor catalytic processes unrelated to weight changes. The thermolysis contribution to CO production was subtracted from the total CO generated in order to analyze the performance of  $\text{La}_{0.6}\text{Sr}_{0.4}\text{Cr}_x\text{Mn}_{1-x}\text{O}_3$  perovskites under isothermal  $\text{CO}_2$  splitting. **Figure 5a** depicts the total CO produced isothermally at 1400 °C, differentiating both sources, thermolysis and  $\text{CO}_2$  splitting. The highest fuel production was observed for  $x = 0.1$ , with  $3.3 \text{ mL g}^{-1}$  of CO, although  $x = 0.3$ – $0.75$  exhibited close performance with CO production around  $2.9 \text{ mL g}^{-1}$ . The compositional ends  $x = 0$  and  $x = 0.85$  showed the lowest production with values below  $2 \text{ mL g}^{-1}$ . Here, it should be pointed out that our cycling tests were designed with shorter exposure to  $\text{CO}_2$  to evaluate the kinetics with respect to the Cr concentration in the perovskite material. It is important to note that the materials are exposed to  $\text{CO}_2$  for 20 min instead of commonly reported 40–60 min in literature.<sup>[10,11]</sup> Because of the shorter oxidation time, the total CO production and  $\text{CO}/\text{O}_2$  molar ratios for  $\text{La}_{0.6}\text{Sr}_{0.4}\text{MnO}_3$  are generally lower when compared to literature. However, for future reactor operation these short time ranges are of relevance, as shorter oxidation times allow for practical reactor operation at increased efficiency.<sup>[11]</sup> It can be seen in Figure 5b that  $\text{La}_{0.6}\text{Sr}_{0.4}\text{MnO}_3$  exhibits a threefold higher oxygen exchange capacity than  $\text{La}_{0.6}\text{Sr}_{0.4}\text{Cr}_{0.85}\text{Mn}_{0.15}\text{O}_3$ . However, this material did not show the highest CO yields because it requires longer exposure to  $\text{CO}_2$ , as previously demonstrated in the literature.<sup>[10,11]</sup> This result illustrates the importance of finding a trade-off between materials with high yields that require short exposure to  $\text{CO}_2$  to affect process efficiency toward flexible operation schemes. Perovskites normally require a larger excess of gaseous oxidant, when compared to that of ceria,<sup>[58]</sup> and it may even be more relevant to assure ideal

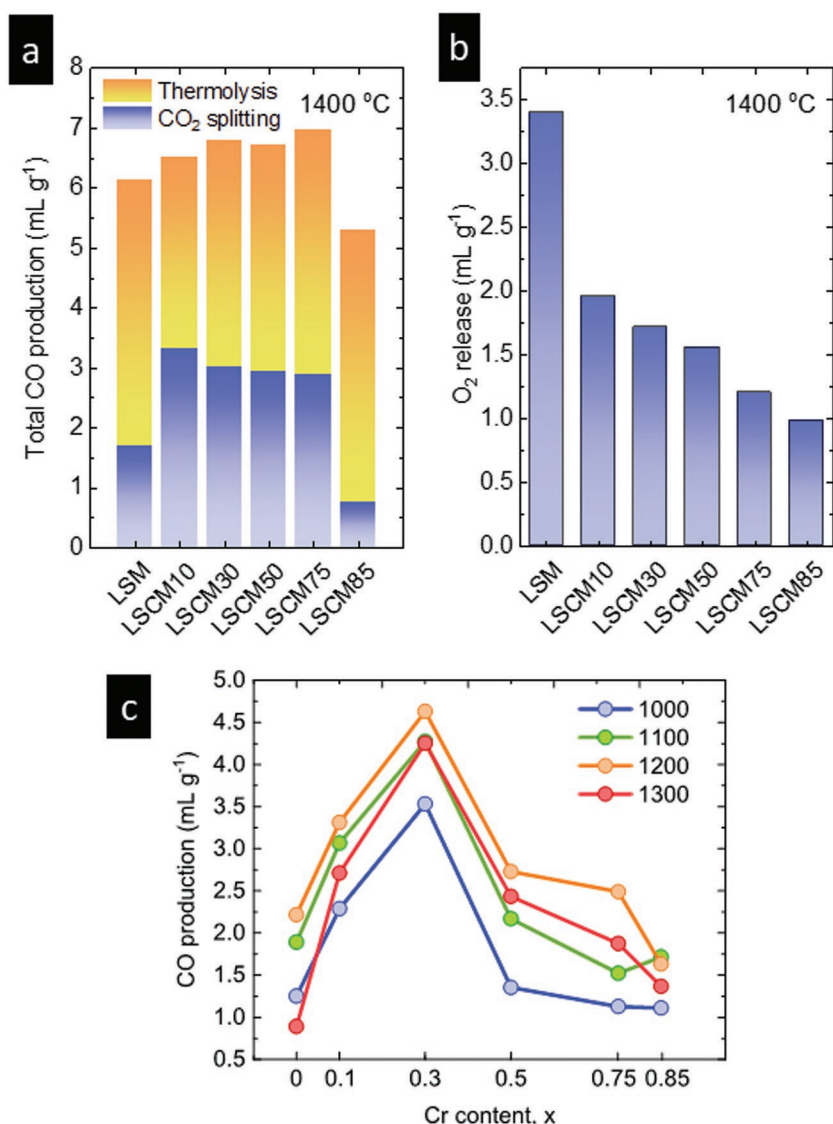


**Figure 5.** a) Total CO production for the isothermal cycle at 1400 °C and  $p_{\text{CO}_2} = 0.5$  atm, differentiating the contribution of the CO produced from the two-step  $\text{CO}_2$ -splitting half-cycle (blue color) and the CO generated via the thermocatalytic cracking of  $\text{CO}_2$  (orange). b) Oxygen release at 1400 and constant flow of Ar 300 mL  $\text{min}^{-1}$ . Values extracted from the integration of the  $\text{O}_2$  curve of the fifth reduction half-cycle. c) Influence of the Cr content,  $x$ , in the CO production for the temperature-swing cycles of  $\text{La}_{0.6}\text{Sr}_{0.4}\text{Cr}_x\text{Mn}_{1-x}\text{O}_3$  perovskites. Only the CO coming from the  $\text{CO}_2$ -splitting reaction is computed.

exposure time in oxidation step. In this respect, under the experimental conditions used for this work, the optimum CO yield production was observed for  $x = 0.3$  at 1200 °C, with 4.6 mL  $\text{g}^{-1}$  (Figure 5c), showing the best CO production under any of the temperature-swing cycling tests conducted, indicating that for such composition a trade-off between oxygen capacity and  $\text{CO}_2$ -splitting rates was attained. Interestingly, for all the compositions the amount of fuel produced at 1300 °C (Figure 5c) was lower than at values obtained at 1200 °C, which for Cr-rich compositions is counterintuitive given the expected increase of fuel yields with temperature on the basis of reported thermodynamic trends in Figure 1. For instance,  $\text{La}_{0.6}\text{Sr}_{0.4}\text{Cr}_{0.75}\text{Mn}_{0.25}\text{O}_3$  shows 2.49 mL  $\text{g}^{-1}$  at 1200 °C, 1.88 mL  $\text{g}^{-1}$  at 1300 °C, and

2.89 mL  $\text{g}^{-1}$  at 1400 °C. Although the general trend indicates that the fuel yield increases with temperature, the value at 1300 °C lies below that trend. We ascribed this anomalous result to the underestimation of CO coming from  $\text{CO}_2$  splitting caused by subtraction of CO coming from the  $\text{CO}_2$  thermolysis source, an effect that is even more pronounced for  $\text{La}_{0.6}\text{Sr}_{0.4}\text{Cr}_{0.85}\text{Mn}_{0.15}\text{O}_3$  due to inherently lower oxygen exchange capacity and smaller fuel increase changes with temperature. Importantly, this fact does not alter the kinetic trends described in the following sections. However, if the amount of CO produced by thermolysis is also computed, then the highest production will be for  $\text{La}_{0.6}\text{Sr}_{0.4}\text{Cr}_{0.75}\text{Mn}_{0.25}\text{O}_3$  at 1400 °C, which is  $\approx 7$  mL  $\text{g}^{-1}$ . Direct thermolysis has been recently tested by Tou et al. and Jiang et al.,<sup>[31,59]</sup> finding in both cases that use of metal oxides that operate on the basis of oxygen vacancy formation enhance the amount of CO produce by direct thermolysis compared to inert materials such as  $\text{Al}_2\text{O}_3$ . The use of a membrane reactor as demonstrated by Tou et al. can be useful for separating the concomitant  $\text{O}_2$  produced by  $\text{CO}_2$  thermolysis.<sup>[31]</sup> Thus, our results suggest that  $\text{La}_{0.6}\text{Sr}_{0.4}\text{Cr}_{0.75}\text{Mn}_{0.25}\text{O}_3$  composition could be a promising candidate to be used as a membrane reactor for redox-augmented direct thermolysis, although some concerns respect to thermodynamic limitations of membrane reactors for direct thermolysis have been raised recently.<sup>[60]</sup>

We turn now to the last five cycles, in order to analyze in more detail, the effect of Cr-incorporation and temperature on the  $\text{CO}_2$ -splitting kinetics. In this case, the reduction temperature was maintained at 1400 °C for every half-cycle in order to guarantee the same extent of oxygen vacancy formation for each temperature at which the  $\text{CO}_2$ -splitting reaction was evaluated. In order to compare more clearly the influence of the Cr content to the kinetics, we plot the CO rate production curve for the samples with the lowest ( $x = 0$  and  $x = 0.1$ ) and highest ( $x = 0.75$  and  $x = 0.85$ ) amount of Cr on the transition metal site, extracted from the  $\text{CO}_2$ -splitting reaction at 1200 °C (Figure 6). It can be observed that for Cr  $x = 0.85$ , a peak rate of 0.93 mL  $\text{min}^{-1}$   $\text{g}^{-1}$  is achieved, which is almost a threefold improvement compared to  $\text{La}_{0.6}\text{Sr}_{0.4}\text{MnO}_3$ , 0.33 mL  $\text{min}^{-1}$   $\text{g}^{-1}$ . A faster kinetic performance is also confirmed by the shorter time needed for reaching equilibrium CO production, which is just 8 min for Cr  $x = 0.85$ , whereas for Cr  $x = 0$  the material did not even reach equilibrium during the 20 min of  $\text{CO}_2$  injection. To put this result in perspective, more commonly used  $\text{La}_{0.6}\text{Sr}_{0.4}\text{MnO}_3$  would require about more than 1 h to reach equilibrium with a fuel production of 8.9 mL  $\text{g}^{-1}$ .<sup>[10]</sup> A peak rate

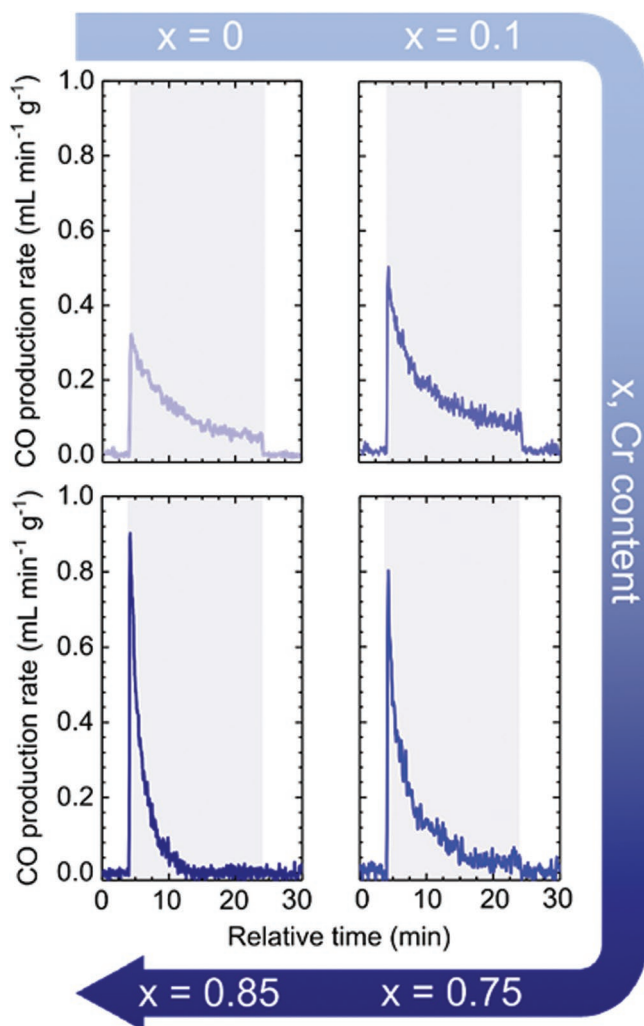


**Figure 6.** CO production rates of  $\text{La}_{0.6}\text{Sr}_{0.4}\text{Cr}_x\text{Mn}_{1-x}\text{O}_3$  materials obtained for the  $\text{CO}_2$ -splitting half-cycle performed at  $1200\text{ }^\circ\text{C}$  and  $p_{\text{CO}_2} = 0.5\text{ atm}$ , previously materials were reduced at  $1400\text{ }^\circ\text{C}$  under Ar atmosphere. Compositional end-members were plotted for the sake of understanding the impact of Cr incorporation in the perovskite. The grey-shaded area indicates the 20 min  $\text{CO}_2$  injection.

of  $0.52\text{ mL min}^{-1}\text{ g}^{-1}$  was observed for the perovskite with Cr content  $x = 0.1$ , however, it also did not reach equilibrium in the given splitting reaction time. In contrast, this was almost achieved by  $\text{La}_{0.6}\text{Sr}_{0.4}\text{Cr}_{0.75}\text{Mn}_{0.25}\text{O}_3$  in the 20 min given for the  $\text{CO}_2$ -splitting reaction, depicting a peak rate value of  $0.8\text{ mL min}^{-1}\text{ g}^{-1}$ . Here, it should be noted that  $\text{La}_{0.6}\text{Sr}_{0.4}\text{Cr}_{0.5}\text{Mn}_{0.5}\text{O}_3$  exhibited a peak rate value that lies below the trend displayed by the other five compositions (Figure S2, Supporting Information). Ignoring this outlier, Figure 6 depicts an increased CO production rate with increasing Cr-incorporation on the transition metal site by comparing the compositional end-members, illustrating the positive influence of Cr-doping on improving the  $\text{CO}_2$ -splitting kinetics. Additionally, the results indicate that it could be possible to design a more efficient material by modulating the Cr-content in order to optimize the  $\text{CO}_2$ -splitting reaction time. This is especially relevant considering the excess of oxidant gas required by perovskites<sup>[58]</sup>

which leads to low  $\text{CO}_2$  to CO total conversions.<sup>[10]</sup> This fact would also affect the CO/ $\text{CO}_2$  separation costs, although Marxer et al. determined it to be 1% of the syngas high heating value.<sup>[61]</sup> In terms of CO/ $\text{CO}_2$  volume concentration peak values range from the highest 1% (v/v) (average 0.2% (v/v) per cycle) for  $\text{La}_{0.6}\text{Sr}_{0.4}\text{Cr}_{0.85}\text{Mn}_{0.15}\text{O}_3$  at  $1400\text{ }^\circ\text{C}$ , to the lowest 0.12% (v/v) (average 0.05% (v/v) per cycle) for  $\text{La}_{0.6}\text{Sr}_{0.4}\text{MnO}_3$  at  $1000\text{ }^\circ\text{C}$ , although it should be noted that experimental conditions were not optimized to favor high CO/ $\text{CO}_2$  volume concentration in the present study. Provided these facts, strategies for more efficient fuel production have been suggested, indicating that limiting the  $\text{CO}_2$ -splitting reaction time would be preferable instead of targeting a maximum fuel output per cycle as preference.<sup>[10]</sup> This trend again points out the need to find perovskite oxides in which not only a high fuel (CO and/or  $\text{H}_2$ ) yield per cycle is achieved, but also materials that exhibit fast  $\text{CO}_2$ -splitting rates, since excess of gaseous reactant is required, which will add energy penalties in the CO/ $\text{CO}_2$  separation.

Next, we analyze the influence of temperature at isothermal and near-isothermal relevant temperatures for the end compositions  $x = 0$  and  $x = 0.85$ , and  $x = 0.5$ , benchmarked against  $\text{CeO}_2$ , the reference material in thermochemical solar-to-fuel production (Figure 7a). For that purpose, commercial  $\text{CeO}_2$ , was subjected to the same thermochemical cycling tests as the perovskite powders (Figure S4, Supporting Information).  $\text{CeO}_2$  is well known to have extremely fast kinetics, especially compared with  $\text{La}_{0.6}\text{Sr}_{0.4}\text{MnO}_3$  materials, which might be considered the reference perovskite material for thermochemical solar-to-fuel production.<sup>[11]</sup> Our experiments revealed that an increase in the  $\text{CO}_2$ -splitting temperature resulted in a remarkable exponential decay of the peak rate for  $\text{CeO}_2$ . Specifically, it decreases by more than three times of its initial rate,  $3.1\text{ mL min}^{-1}\text{ g}^{-1}$  at  $1200\text{ }^\circ\text{C}$ , to  $0.8\text{ mL min}^{-1}\text{ g}^{-1}$  at  $1400\text{ }^\circ\text{C}$ , keeping the reduction temperature at  $1400\text{ }^\circ\text{C}$  in both cases. Contrarily,  $\text{La}_{0.6}\text{Sr}_{0.4}\text{Cr}_x\text{Mn}_{1-x}\text{O}_3$  materials improved their kinetic performance with an increase of the  $\text{CO}_2$ -splitting temperature in a linear fashion.

In this work we report first temperature-dependent kinetic trends for perovskites of the family  $\text{La}_{0.6}\text{Sr}_{0.4}\text{Cr}_x\text{Mn}_{1-x}\text{O}_3$  at near-isothermal and isothermal regimes. Most of current literature investigates perovskite oxides only in temperature-swung cycling operation. For example, we only found a similar work for hercynite, which exhibited faster  $\text{CO}_2$ -splitting rates with increased isothermal temperature,<sup>[56]</sup> ascribed to a higher reduction extent with increased temperature. Authors argued that a higher reduction extent increases the oxidation driving force due to an enhanced favorability for CO production. This kinetic behavior reported by Muhich et al., matches well for both the perovskite (Figure S2, Supporting Information) and ceria (Figure S4, Supporting Information), behavior with increasing isothermal temperature, that is the three first cycles of our thermochemical cycling program. Interestingly, this behavior does not apply for ceria when cycled between two different temperatures, i.e.,  $T_{\text{red}} = 1400\text{ }^\circ\text{C}$  and  $T_{\text{ox}} = 1000\text{--}1300\text{ }^\circ\text{C}$ . In this case, the reduction extent is to some degree fixed, and ceria shows a higher favorability for splitting  $\text{CO}_2$  at lower temperatures, exhibiting a slowdown when the oxidation temperature is increased as shown in Figure 7a. This is ascribed to the thermodynamics of ceria, which shows a high gain in

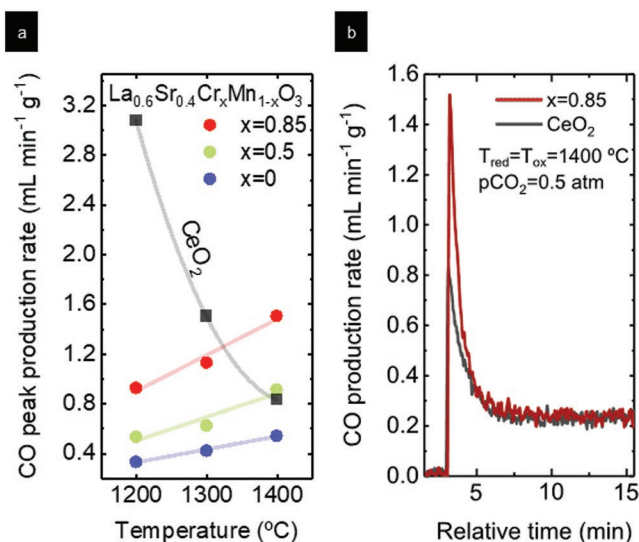


**Figure 7.** a) CO production rate peak values determined at temperatures relevant to near- and isothermal splitting cycles. Here, the oxides were previously reduced at 1400 °C under Ar atmosphere and then cooled down (or maintained) to the CO<sub>2</sub>-splitting temperature, 1200–1400 °C. For the sake of comparison, results for the compositional end-members, La<sub>0.6</sub>Sr<sub>0.4</sub>MnO<sub>3</sub> (LSM) and La<sub>0.6</sub>Sr<sub>0.4</sub>Cr<sub>0.85</sub>Mn<sub>0.15</sub>O<sub>3</sub> (LSCM85); La<sub>0.6</sub>Sr<sub>0.4</sub>Cr<sub>0.5</sub>Mn<sub>0.5</sub>O<sub>3</sub> (LSCM50) and CeO<sub>2</sub> are plotted. Fitting curves are just used as a visual guide. b) Comparison of the CO production profiles of La<sub>0.6</sub>Sr<sub>0.4</sub>Cr<sub>0.85</sub>Mn<sub>0.15</sub>O<sub>3</sub> (LSCM85) and commercial ceria at 1400 °C. Note that the catalytic contribution of CO<sub>2</sub> thermolysis has not been subtracted for the sake of comparison.

thermodynamic driving force with cooling,<sup>[62]</sup> that is, faster CO rates at lower temperatures and decay at high temperatures (1000–1400 °C) as shown in Figure 7a and Figure S4 in the Supporting Information, corroborating the trends reported by Davenport et al.<sup>[63]</sup> On the other hand, the La<sub>0.6</sub>Sr<sub>0.4</sub>Cr<sub>x</sub>Mn<sub>1-x</sub>O<sub>3</sub> series exhibit the opposite behavior.

Fundamentally this finding is in line with the theoretical trend illustrated in Figure 1 that depicts an increased CO<sub>2</sub>-splitting thermodynamic driving force,  $\Delta G_{\text{rxn}}$ , for samples with high chromium content in the high temperature regime. Turning to Figure 7a again, it can be seen that the rate enhancement with temperature can be ranked in the following way:  $x = 0.85 > x = 0.5 > x = 0$ ; which can be observed by a steeper slope for the linear trend of CO rates with temperature (red, green and blue lines, respectively). While this corroborates that the driving force gain is higher for Cr-rich perovskites than for La<sub>0.6</sub>Sr<sub>0.4</sub>MnO<sub>3</sub>, it would be expected a higher CO production rate difference in favor of  $x = 0.85$  at high temperatures, and increased rate values for La<sub>0.6</sub>Sr<sub>0.4</sub>MnO<sub>3</sub> when decreasing the temperature. One possible reason for this behavior can be explained by the rationale of Muhich et al., mentioned above, which ascribed higher CO<sub>2</sub>-splitting driving force for increased reduction extents for hercynite. Here, we note that for temperature-swing cycles, the higher the temperature difference between  $T_{\text{red}}$  and  $T_{\text{ox}}$ , the longer it took to reach the set-point oxidation temperature. Namely, it took  $\approx 20$  min to cool down from 1400 to 1000 °C, while just 2 min from 1400 to 1300 °C. Although the same cooling rate was programed for both, 50 °C min<sup>-1</sup>, the electric-furnace thermal inertia caused

an exponential cooling down; see the top-panel in Figure S2 in the Supporting Information, which delayed reaching 1000 °C by 12 min more. During cooling, the metal oxide will be reoxidized slightly from residual oxygen in the inert gas stream, which decreases the reduction extent  $\delta$  before CO<sub>2</sub> splitting, phenomenon previously reported by Cooper et al.,<sup>[57]</sup> being this alteration negligible for near-isothermal schemes. Other authors avoided this artifact by using rapid-cooling IR furnaces.<sup>[10]</sup> This hypothesis could serve to explain why the reported CO yields (Figure 5a) are much lower for 1000 °C. Reoxidation will also affect the reduction extent of ceria but less on its reoxidation kinetics (Figure 7a and Figure S4 in the Supporting Information). The reason is again explained by thermodynamic trends, since the driving force for CO<sub>2</sub> splitting for ceria strongly increases with decreasing the temperature, while the driving force for splitting is not affected to the same degree by lowering the oxygen nonstoichiometry,  $\delta$ .<sup>[62]</sup> This fact once more emphasizes the importance of the reported trends in this work. That is, for the isothermal reactor operation, in which  $T_{\text{red}} = T_{\text{ox}} = 1400$  °C, La<sub>0.6</sub>Sr<sub>0.4</sub>Cr<sub>0.85</sub>Mn<sub>0.15</sub>O<sub>3</sub> exhibits a twofold faster fuel production rate compared to CeO<sub>2</sub>, being at 1.5 and 0.8 mL min<sup>-1</sup> g<sup>-1</sup>, respectively (Figure 7b). This result indicates that by adjusting both the perovskite composition and reactor operational scheme, it is possible to find material alternatives that outperform state-of-the-art perovskites, such as La<sub>0.6</sub>Sr<sub>0.4</sub>MnO<sub>3</sub>, and more importantly, ceria. Thus, it is demonstrated that La<sub>0.6</sub>Sr<sub>0.4</sub>Cr<sub>x</sub>Mn<sub>1-x</sub>O<sub>3</sub> solid solutions are promising candidates for renewable fuel production at isothermal and near-isothermal operation. Importantly, such cycling schemes will reduce process downtimes (cooling down), avoid solid–solid heat recuperation, and mitigate thermal stresses, for both the reactor and redox material.<sup>[35]</sup>

In order to assess the microstructural and crystallographic stability, XRD, SEM, and energy dispersive X-ray spectroscopy (EDX) were performed to the samples after the cycling tests. XRD analyses (Figure S5, Supporting Information) confirmed that the rhombohedral perovskite structure is the single phase present after cycling, without further evidence of phase segregation for all the Cr-doped,  $x = 0.1$ – $0.85$ , La<sub>0.6</sub>Sr<sub>0.4</sub>Cr<sub>x</sub>Mn<sub>1-x</sub>O<sub>3</sub> perovskite materials. Furthermore, the cell volume values remained almost constant after cycling, and following the same trend as for the pristine samples (Figure 3a) for all the compositional series denoting high crystallographic stability. Upon cycling, SEM micrographs (Figure 4i–h) revealed that Cr-doped materials showed remarkable morphological stability given the prolonged thermochemical treatment at high temperatures, except for La<sub>0.6</sub>Sr<sub>0.4</sub>MnO<sub>3</sub> (Figure 4g) whose particles grow from  $1.5 \pm 0.5$   $\mu\text{m}$  before cycling to  $3 \pm 0.5$   $\mu\text{m}$  after the thermochemical cycling tests. Interestingly, La<sub>0.6</sub>Sr<sub>0.4</sub>MnO<sub>3</sub> was composed of a smaller average grain size ( $1.5 \pm 0.5$   $\mu\text{m}$  vs  $2.5 \pm 0.7$   $\mu\text{m}$  for La<sub>0.6</sub>Sr<sub>0.4</sub>Cr<sub>0.3</sub>Mn<sub>0.7</sub>O<sub>3</sub>), more bimodal distribution, some closed porosity and a higher rounding degree of the sintered particles as depicted in Figure 4a. This observation is important, since this composition exhibited the slowest CO production at the isothermal test conditions. This result denotes that a lower level of compaction exists for the undoped chromium case of the perovskite revealing a smaller grain size and also

a more open microstructure. This accounts for higher surface areas, however, in this case, it does not necessarily correlate with faster kinetics. This fact indicates that at the high temperatures of the isothermal CO<sub>2</sub>-splitting cycles, the reaction is less controlled by diffusion or surface kinetics, but highly influenced by thermodynamic driving forces. However, an additional study assessing surface modifications of these materials should be performed to corroborate the aforementioned observations.

Furthermore, the presence of small precipitates was observed along some grain boundaries, although the low concentration prevents from detection of such phase using XRD (Figure S5, Supporting Information). Based on the observed lower degree of morphological alteration after the severe thermochemical cycling, we could conclude that Cr-doping could be beneficial in preventing sintering-related effects. These results together with the microstructural durability of La<sub>0.6</sub>Sr<sub>0.4</sub>Cr<sub>x</sub>Mn<sub>1-x</sub>O<sub>3</sub> powders with  $x = 0.1-0.85$  suggests the beneficial effect of Cr-doping preventing materials degradation at high-temperature thermochemical cycling conditions.

### 2.3. Longevity Test under High-Temperature Isothermal Cycling

Finally, the thermochemical longevity performance of the La<sub>0.6</sub>Sr<sub>0.4</sub>Cr<sub>x</sub>Mn<sub>1-x</sub>O<sub>3</sub> materials was tested under 15 isothermal redox cycles carried out for La<sub>0.6</sub>Sr<sub>0.4</sub>Cr<sub>0.85</sub>Mn<sub>0.15</sub>O<sub>3</sub> at 1400 °C (Figure 8a). Here, it can be observed that after the first four cycles, CO production rates stabilized around values of  $1.65 \pm 0.05 \text{ mL min}^{-1} \text{ g}^{-1}$ , which lies in the range of the CO<sub>2</sub>-splitting rates observed for the same material at 1400 °C (Figure 7). This fact illustrates the reproducibility of the splitting results and the remarkable kinetic stability of La<sub>0.6</sub>Sr<sub>0.4</sub>Cr<sub>0.85</sub>Mn<sub>0.15</sub>O<sub>3</sub> under high-temperature isothermal CO<sub>2</sub>-splitting cycling schemes. Interestingly, the area under the tail of the CO signal decreased with cycling, an effect that was more pronounced during the first four cycles. This result indicates a cycle-to-cycle decline in the amount of CO produced by thermolysis. The fact that the CO originated by thermocatalytic splitting decreases with time might be ascribed to a reduction of active perovskite surface due to high-temperature sintering effects.

SEM was used in order to analyze the microstructural changes after such prolonged isothermal cycling test and explore this hypothesis. The morphology evolution is depicted in Figure 8b,c, depicting La<sub>0.6</sub>Sr<sub>0.4</sub>Cr<sub>0.85</sub>Mn<sub>0.15</sub>O<sub>3</sub> before and after the 15 cycles, respectively. The comparison of the two micrographs shows that after cycling, the particle grains exhibited an enhanced rounding degree (Figure 8c) in comparison with the sharper edges before cycling (Figure 8b). This result could explain the aforementioned lower thermocatalytic activity since the rounded particles might have less active sites for CO<sub>2</sub> thermolysis due to the partial decrease of surface area. The average grain size values of both the material before and after cycling lie around the same values,  $1.7 \pm 0.6 \mu\text{m}$ , which might indicate that, besides the grain rounding, La<sub>0.6</sub>Sr<sub>0.4</sub>Cr<sub>0.85</sub>Mn<sub>0.15</sub>O<sub>3</sub> maintains remarkable microstructural stability after 15 isothermal CO<sub>2</sub>-splitting redox cycles at

1400 °C. Durability is also crucial, considering that redox materials for solar-driven thermochemical syngas production are going to be exposed to long-term cycling at high temperatures, in order to guarantee the feasibility of the process. EDX elemental mapping performed to La<sub>0.6</sub>Sr<sub>0.4</sub>Cr<sub>0.85</sub>Mn<sub>0.15</sub>O<sub>3</sub> revealed a uniform ionic distribution after the 15 redox isothermal cycles (Figure 8d). Additionally, XRD confirmed that rhombohedral perovskite is the solely crystal phase present in the material after the durability test at 1400 °C (Figure S6, Supporting Information).

XPS was also used to compare the chemical stability and to probe any changes in the valence states and their proportions in La<sub>0.6</sub>Sr<sub>0.4</sub>Cr<sub>0.85</sub>Mn<sub>0.15</sub>O<sub>3</sub> prior to and after 15 isothermal cycles carried out isothermally at the maximum temperature of 1400 °C. In particular, we focus on the high-resolution XPS of the Cr2p<sub>1/2</sub> and Cr2p<sub>3/2</sub>; and Mn2p<sub>3/2</sub> and Mn2p<sub>1/2</sub> regions in order to study the surface stability of the multivalent redox cations present in the perovskite (Figure 8e). Each Cr2p spectrum was fitted using spin-orbital doublets centered at 576.1 and 585.9 eV ascribed respectively to Cr2p<sub>3/2</sub> and Cr2p<sub>1/2</sub> of Cr<sup>3+</sup>, spin-orbital doublets centered at 577.1 and 586.8 eV attributed respectively to Cr2p<sub>3/2</sub> and Cr2p<sub>1/2</sub> of Cr<sup>4+</sup>, and spin-orbital doublets centered at 580.0 and 589.5 eV, respectively due to Cr2p<sub>3/2</sub> and Cr2p<sub>1/2</sub> of Cr<sup>6+</sup>.<sup>[64,65]</sup> Importantly, the presence of Cr<sup>4+</sup>, in both the cycled and the pristine samples, confirms our XRD and Raman observations, that implied an increasing presence of Cr<sup>4+</sup> with increasing incorporation of Cr in the as-prepared perovskites, see Section 2.1. The presence of Cr<sup>6+</sup> has been previously reported in Cr-perovskites under oxidative conditions,<sup>[41]</sup> which in this case is very minor since SrCrO<sub>4</sub> was not detected by XRD either in the pristine material (Figure 2) or in the cycled form (Figures S5 and S6, Supporting Information). Comparing the spin orbitals peak position of the pristine versus cycled samples, it can be observed negligible differences in the oxidation state of Cr on the surface of La<sub>0.6</sub>Sr<sub>0.4</sub>Cr<sub>0.85</sub>Mn<sub>0.15</sub>O<sub>3</sub> before and after isothermal cycling (Figure 8e). Conversely, differences between the as-prepared and cycled La<sub>0.6</sub>Sr<sub>0.4</sub>Cr<sub>0.85</sub>Mn<sub>0.15</sub>O<sub>3</sub> exist in the oxidation state of Mn, as shown by the Mn2p spectra in Figure 8e. Here, each Mn2p spectrum was fitted with spin-orbital doublets centered at 641.3 and 652.5 eV (full width at half maximum (FWHM) = 2.4 eV), respectively due to Mn2p<sub>3/2</sub> and Mn2p<sub>1/2</sub> of Mn<sup>3+</sup> and spin-orbital doublets centered at 643.0 and 654.2 eV (FWHM = 2.4 eV), respectively ascribed to Mn2p<sub>3/2</sub> and Mn2p<sub>1/2</sub> of Mn<sup>4+</sup>.<sup>[66,67]</sup> The valence state of Mn was roughly 50:50 for Mn<sup>4+</sup> and Mn<sup>3+</sup> in as-synthesized La<sub>0.6</sub>Sr<sub>0.4</sub>Cr<sub>0.85</sub>Mn<sub>0.15</sub>O<sub>3</sub> (Figure 8e). On the other hand, there was ≈20% increase in Mn<sup>4+</sup> after 15 isothermal cycles; this increase in Mn valence could be a result of the high temperature for isothermal cycling as well as the oxidative environment at which the material is exposed in the last part of the longevity test (50% CO<sub>2</sub>). The La3d and Sr3d spectra reveal that the valence of both La (e.g., La<sup>3+</sup>) and Sr (e.g., Sr<sup>2+</sup>) are consistent in as-prepared and cycled La<sub>0.6</sub>Sr<sub>0.4</sub>Cr<sub>0.85</sub>Mn<sub>0.15</sub>O<sub>3</sub> (Figure S7, Supporting Information). This result implies that Mn ions, along with Cr ions, are the active redox sites that participate in the oxygen exchange during thermochemical CO<sub>2</sub> splitting. Still, the valence states of La, Sr, and Cr are largely unchanged before and after the longevity test, which supports the observed retention in the redox activity

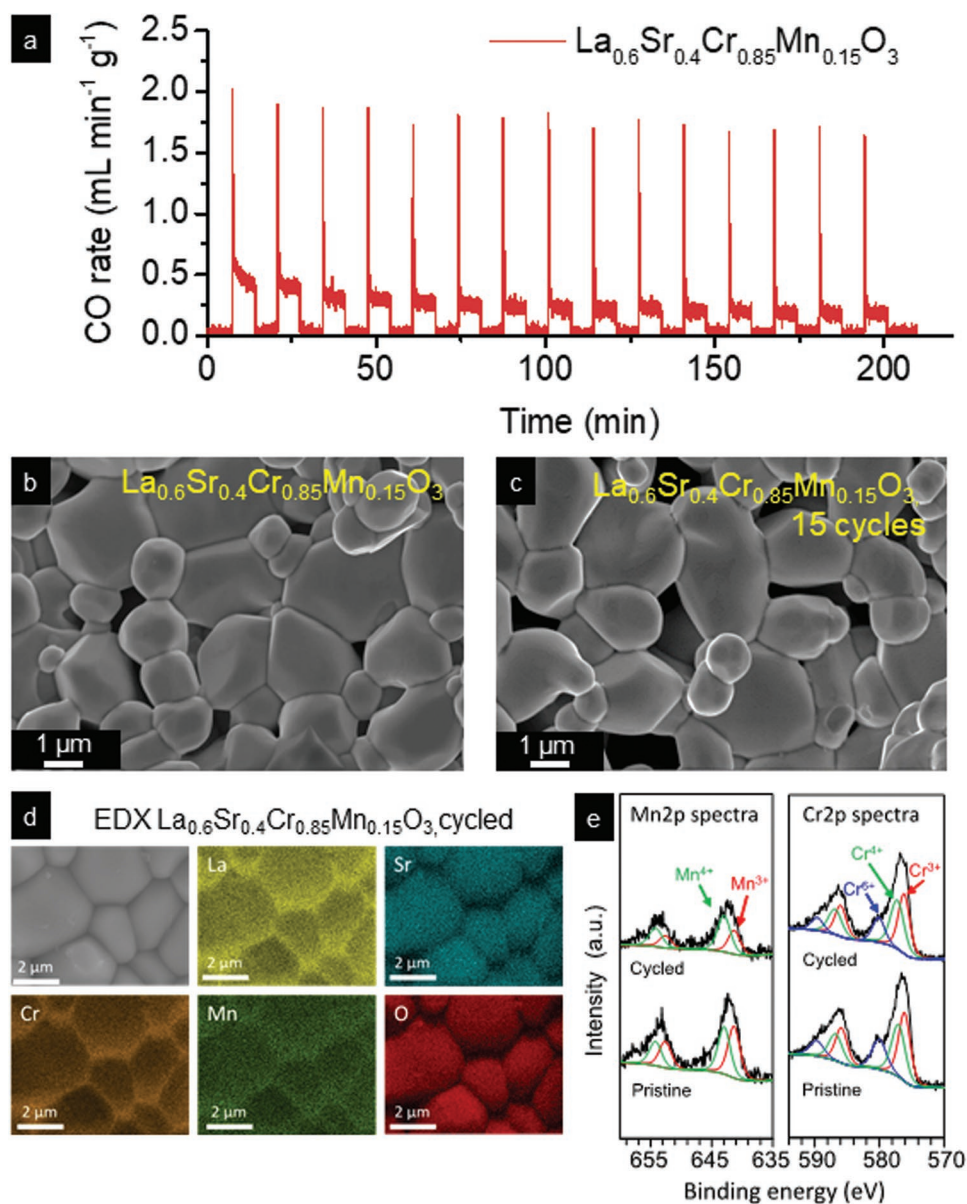


**Figure 8.** a) CO production rate observed during a longevity test carried out for  $\text{La}_{0.6}\text{Sr}_{0.4}\text{Cr}_{0.85}\text{Mn}_{0.15}\text{O}_3$  consisting of 15 isothermal cycles at 1400 °C. Reduction was performed under Ar atmosphere and  $\text{CO}_2$ -splitting steps using a mixture of 50%  $\text{CO}_2$  balanced with Ar, maintaining always the flow at 300  $\text{mL min}^{-1}$ . b,c) SEM micrographs comparing the morphology between as-synthesized and cycled  $\text{La}_{0.6}\text{Sr}_{0.4}\text{Cr}_{0.85}\text{Mn}_{0.15}\text{O}_3$ . d) EDX mapping of the cycled  $\text{La}_{0.6}\text{Sr}_{0.4}\text{Cr}_{0.85}\text{Mn}_{0.15}\text{O}_3$ . e) Mn2p and Cr2p XPS comparison between  $\text{La}_{0.6}\text{Sr}_{0.4}\text{Cr}_{0.85}\text{Mn}_{0.15}\text{O}_3$  before and after cycling.

of  $\text{La}_{0.6}\text{Sr}_{0.4}\text{Cr}_{0.85}\text{Mn}_{0.15}\text{O}_3$ . Thus, based on the 15 isothermal cycles test and the high degree of surface and microstructural stability corroborated by XPS, SEM, XRD, and EDX, we can conclude that  $\text{La}_{0.6}\text{Sr}_{0.4}\text{Cr}_{0.85}\text{Mn}_{0.15}\text{O}_3$  shows promise for thermochemical solar-to-fuel production at high temperatures.

### 3. Conclusions

Thermochemical fuel production suitable for solar-driven reactors was operated on the basis of the new  $\text{La}_{0.6}\text{Sr}_{0.4}\text{Cr}_x\text{Mn}_{1-x}\text{O}_3$  perovskite materials, which exhibit promising  $\text{CO}_2$  fuel-split-

ting rates at higher operation temperature for an increase in Cr-doping. The most favorable rate performance was observed for  $\text{La}_{0.6}\text{Sr}_{0.4}\text{Cr}_{0.85}\text{Mn}_{0.15}\text{O}_3$ , which showed twofold faster  $\text{CO}_2$ -splitting reaction than state-of-the-technology ceria, 1.5 and 0.8  $\text{mL min}^{-1} \text{g}^{-1}$ , respectively, when operated under isothermal cycles at 1400 °C. Furthermore, this material showed high thermochemical and structural stability and durability when tested under a 15 multicycle isothermal test at 1400 °C. Surface analysis of  $\text{La}_{0.6}\text{Sr}_{0.4}\text{Cr}_{0.85}\text{Mn}_{0.15}\text{O}_3$  displayed small differences in the valence states of La, Sr, Cr, and Mn before and after 15 isothermal cycles, implying that these perovskites mostly retain their surface chemistry under the reaction conditions, which

is critical since Mn and Cr ions are the redox-active sites that participate in the oxygen exchange during the thermochemical cycling. These results support the hypothesis that an enhanced thermodynamic driving force to split CO<sub>2</sub> exists, with increased Cr-content for the lanthanum strontium chromium manganese perovskites. Regarding the total fuel production, the optimal composition is La<sub>0.6</sub>Sr<sub>0.4</sub>Cr<sub>x</sub>Mn<sub>1-x</sub>O<sub>3</sub> operated under near-isothermal conditions,  $T_{\text{red}} = 1400\text{ °C}/T_{\text{ox}} = 1200\text{ °C}$ , which are also more efficient than pure isothermal cycling in terms of heat recuperation, excess of CO<sub>2</sub> needed and the operational mode for the reduction step.<sup>[35]</sup>

In summary, we demonstrate on the example of La<sub>0.6</sub>Sr<sub>0.4</sub>Cr<sub>x</sub>Mn<sub>1-x</sub>O<sub>3</sub> that one can adapt the perovskite chemistry (i.e., doping of transition metal ions) to tune the thermochemical properties in order to meet the most optimum trade-off between fast kinetics and fuel production, which can also benefit from the most suitable near-isothermal/isothermal reactor schemes conditions. These are thus promising material candidates for solar-driven thermochemical fuel production and may give perspective to alternative reactor operation schemes.

## 4. Experimental Section

**Material Preparation:** La<sub>0.6</sub>Sr<sub>0.4</sub>Cr<sub>x</sub>Mn<sub>1-x</sub>O<sub>3</sub> solid solutions ( $0 \leq x \leq 0.85$ ) were synthesized using a modified version of the Pechini method. Citric acid (Sigma Aldrich, ≥99%) together with stoichiometric amounts of nitrate precursors, namely La(NO<sub>3</sub>)<sub>3</sub>·6H<sub>2</sub>O (Sigma Aldrich, ≥99.99%), Sr(NO<sub>3</sub>)<sub>2</sub> (Fluka Analytical, ≥99%), Cr(NO<sub>3</sub>)<sub>2</sub>·9H<sub>2</sub>O (Sigma Aldrich, ≥97%), and Mn(NO<sub>3</sub>)<sub>2</sub>·4H<sub>2</sub>O (Sigma Aldrich, ≥97%) was dissolved in deionized water at room temperature in a 60:40 ratio. Afterward, the aqueous solution was heated up to 80 °C under constant stirring, followed by addition of ethylene glycol (Fluka Analytical, ≥98%) in a 2 to 3 weight ratio. Continuing the stirring and keeping the temperature at 80 °C, water was evaporated until a gel was formed. The gel was then dried on a heating plate at 200 °C for 2 h followed by calcination for 1 h at 400 °C. The calcined gel was ground to fine powders in an agate mortar, and heat-treated inside an alumina crucible at 1250 °C for 10 h, setting a heating rate of 20 °C min<sup>-1</sup>. In order to avoid undesired chromate segregations, materials were calcined further at 1400 °C for 24 h. A list of the synthesized materials is given in Table 1. Commercial CeO<sub>2</sub> (Sigma Aldrich, nanopowder with an average grain size of 50 nm, 99.95% purity) was employed as a benchmark.

**Materials Physicochemical Characterization:** X-ray powder diffraction data were collected with a Panalytical X'Pert PRO MPD diffractometer. Cu K $\alpha$  radiation ( $\lambda = 1.5406\text{ \AA}$ ; Ge monochromator) produced with an extraction voltage of 45 kV at 40 mA current was used to scan the samples in a Bragg–Brentano geometry in the range of  $20^\circ < 2\theta < 120^\circ$  with a spinning speed of 60 rot min<sup>-1</sup>, a step width of 0.017°, and irradiation time of 3 s. Panalytical HighScore Plus software was utilized for Rietveld fitting, considering a rhombohedral perovskite (165744-ICSD) model structure and fitting the experimental data with a Pseudo Voigt function.

Raman spectra were collected on a confocal WITec Alpha300 R Raman microscope instrument (WITec Germany) equipped with 532 nm laser, using the 100-fold magnification objective and laser power of 0.5 or 1 mW, with a spectral resolution of 0.36 cm<sup>-1</sup>. Each single spectrum consisted of three accumulations with an integration of 10 s.

The microstructure and particle morphology were assessed on a Zeiss Merlin High-resolution SEM. An acceleration voltage of 7 kV and Inlens detector were used. The same equipment was used for elemental characterization via EDX with an Octane Elect EDS System. The average particle size was determined using the software ImageJ.<sup>[68]</sup>

TGA were carried out on a NETZSCH 449C equipped with a set of mass flow controllers (Bronkhorst) allowing atmospheric control during the experiments. In order to determine the reduction extent ( $\delta$ ) of La<sub>0.6</sub>Sr<sub>0.4</sub>Cr<sub>x</sub>Mn<sub>1-x</sub>O<sub>3</sub> solid solutions, about 100 mg of perovskite powders were placed in a TGA alumina crucible and heated up to 1400 °C under constant Ar flow of 100 mL min<sup>-1</sup>, with heating and cooling rates of 20 °C min<sup>-1</sup>.

XPS was performed on a Thermo K-Alpha XPS system with a spot size of 400  $\mu\text{m}$  and a resolution of 0.1 eV. All spectra were processed and analyzed using Thermo Avantage, which is a software package provided through ThermoScientific; the FWHM doublet splittings (where applicable), and peak positions were constant and fixed for all XPS deconvolutions.

**Thermochemical Cycling:** The capacity of La<sub>0.6</sub>Sr<sub>0.4</sub>Cr<sub>x</sub>Mn<sub>1-x</sub>O<sub>3</sub> solid solutions for two-step thermochemical CO<sub>2</sub> production was evaluated in a high-temperature fixed-bed reactor connected to a Raman laser gas analyzer (Atmospheric Recovery, Inc.). Figure S8 in the Supporting Information illustrates the experimental reactor setup. It consists of a set of electric mass flow controllers (Voegtlin) that adjusted the desired gas compositions of inert or oxidizing gas to the alumina reactor (Nanoker, 800 mm length, 12 mm outer diameter), located inside a vertical tubular electrical furnace (HTRV 16/40/250/E3216CP/OTC, Carbolite Gero GmbH). About 1 g of perovskite material was placed in powder form over an alumina porous wool bed situated at the half-length of the alumina tube. Sample temperature was monitored by an S-type thermocouple in contact with the outer surface of the perovskite powder loose bed. The outlet gas stream was analyzed by a Raman laser gas analyzer, calibrated with premixed gas cylinders of known concentrations (zero gas bottle of Ar; reducing gas bottle 0.5% CH<sub>4</sub>, 0.5% H<sub>2</sub>, 0.5% CO balanced with Ar; oxidizing gas bottle with 5% O<sub>2</sub>, 15% CO<sub>2</sub>, balanced with N<sub>2</sub>, all 99.9999%, Airgas).

Thermochemical cycling runs for CO<sub>2</sub> splitting were specifically programmed for the evaluation of the temperature influence on the CO production kinetics. For that purpose, La<sub>0.6</sub>Sr<sub>0.4</sub>Cr<sub>x</sub>Mn<sub>1-x</sub>O<sub>3</sub> powder materials were screened under a cycling program consisting of eight alternating reduction and oxidation cycles. Before each experiment, a purging step with Ar was carried out to remove residual ambient air coming from off-operation periods. Then, the first three cycles evaluated the CO<sub>2</sub>-splitting behavior at three isothermal temperatures (1200, 1300, 1400 °C). After reaching the desired temperature, the reduction was performed for 30 min under a constant flow of 300 mL min<sup>-1</sup> of Ar (99.999% purity, Airgas). The total gas flow was always kept at this value based on the gas analyzer specifications. After the reduction step, CO<sub>2</sub> (99.998%, Airgas) balanced with Ar was injected at a  $p_{\text{CO}_2} = 0.5\text{ atm}$ . The second part of the cycling test was performed under a temperature-swing scheme. Reduction was carried out at 1400 °C for 20 min, after which the temperature was cooled down to the desired value for the CO<sub>2</sub> splitting. After reaching the programmed temperatures (1000, 1100, 1200, 1300 °C), CO<sub>2</sub> was injected at the same concentration as for the three first cycles during 20 min. Finally, the material was subjected to a last isothermal cycle at 1400 °C. For every heating ramp, 50 °C min<sup>-1</sup> rates were used. The CO total production was obtained by integration of the CO production curves. For CO<sub>2</sub> splitting at high temperatures (1300–1400 °C) the amount of CO generated by CO<sub>2</sub> thermolysis (CO<sub>2</sub>(g) → CO + ½ O<sub>2</sub>(g)) was subtracted from the total CO produced by computing the O<sub>2</sub> produced during the thermolysis and obtaining the equivalent stoichiometric amount of CO, which was then subtracted from the total CO yield.

## Supporting Information

Supporting Information is available from the Wiley Online Library or from the author.

## Acknowledgements

The authors acknowledge financial support by the ETH Foundation for this work (grant number ETH-05 13-1). The authors would like to

thank Dr. R. Pfenninger for developing the setup control software, Patrick Boisvert for the help with EDX and Dr. C. Settens for the initial help with XRD refinement. This work made use of the MRSEC Shared Experimental Facilities at MIT, supported by the National Science Foundation under award number DMR-14-19807. In addition, the authors thank Prof. A. Studart, ETH Zurich, for the use of the TGA. A.J.C., A.H.B., and J.L.M.R. conceived the project. A.H.B. performed the thermodynamic calculations and interpretation. T.M. synthesized the materials. A.J.C. designed and built the reactor setup with help of A.H.B. and T.M. T.M. and A.J.C. performed the reactor experiments, XRD, EDX, and SEM. T.M. performed the TGA. T.M. and E.S. performed the Raman characterization and interpretation. Z.D.H. performed the XPS characterization and interpretation. J.L.M.R. discussed and supervised the work. The paper was co-written by A.J.C., A.H.B. and J.L.M.R., and all authors discussed the results and commented on the manuscript.

## Conflict of Interest

The authors declare no conflict of interest.

## Keywords

isothermal, kinetics, perovskites, solar fuels, thermochemical

Received: December 17, 2018

Revised: May 30, 2019

Published online:

- [1] H. L. Tuller, *Mater. Renewable Sustainable Energy* **2017**, 6, 3.
- [2] C. N. R. Rao, S. Dey, *Proc. Natl. Acad. Sci. USA* **2017**, 114, 13385.
- [3] R. J. Carrillo, J. R. Scheffe, *Sol. Energy* **2017**, 156, 3.
- [4] A. H. McDaniel, *Curr. Opin. Green Sustainable Chem.* **2017**, 4, 37.
- [5] C. L. Muhich, B. D. Ehrhart, I. Al-Shankiti, B. J. Ward, C. B. Musgrave, A. W. Weimer, *Wiley Interdiscip. Rev.: Energy Environ.* **2016**, 5, 261.
- [6] D. Marner, P. Furler, M. Takacs, A. Steinfeld, *Energy Environ. Sci.* **2017**, 10, 1142.
- [7] S. Zhai, J. Rojas, N. Ahlborg, K. Lim, M. F. Toney, H. Jin, W. C. Chueh, A. Majumdar, *Energy Environ. Sci.* **2018**, 11, 2172.
- [8] M. Kubicek, A. H. Bork, J. L. M. Rupp, *J. Mater. Chem. A* **2017**, 5, 11983.
- [9] J. R. Scheffe, D. Weibel, A. Steinfeld, *Energy Fuels* **2013**, 27, 4250.
- [10] C.-K. Yang, Y. Yamazaki, A. Aydin, S. M. Haile, *J. Mater. Chem. A* **2014**, 2, 13612.
- [11] M. J. Ignatowich, A. H. Bork, T. C. Davenport, J. L. M. Rupp, C. Yang, Y. Yamazaki, S. M. Haile, *MRS Commun.* **2017**, 7, 873.
- [12] A. H. Bork, E. Povoden-Karadeniz, J. L. M. Rupp, *Adv. Energy Mater.* **2017**, 7, 1601086.
- [13] S. Dey, B. S. Naidu, C. N. R. Rao, *Dalton Trans.* **2016**, 45, 2430.
- [14] S. Dey, B. S. Naidu, A. Govindaraj, C. N. R. Rao, *Phys. Chem. Chem. Phys.* **2015**, 17, 122.
- [15] S. Dey, B. S. Naibu, C. N. R. Rao, *Chem. - Eur. J.* **2015**, 21, 7077.
- [16] A. Demont, S. Abanades, *RSC Adv.* **2014**, 4, 54885.
- [17] A. Demont, S. Abanades, *J. Mater. Chem. A* **2015**, 3, 3536.
- [18] J. Vieten, B. Bulfin, P. Huck, M. Horton, D. Guban, L. Zhu, Y. Lu, K. A. Persson, M. Roeb, C. Sattler, *Energy Environ. Sci.* **2019**, 12, 1369.
- [19] D. R. Barcellos, M. D. Sanders, J. Tong, A. H. McDaniel, R. P. O'Hayre, *Energy Environ. Sci.* **2018**, 11, 3256.
- [20] A. Riaz, P. Kreider, F. Kremer, H. Tabassum, J. S. Yeoh, W. Lipirski, A. Lowe, *ACS Appl. Energy Mater.* **2019**, 2, 2494.
- [21] D. Papargyriou, J. T. S. Irvine, *Solid State Ionics* **2016**, 288, 120.
- [22] S. Tao, J. T. S. Irvine, *J. Electrochem. Soc.* **2004**, 151, A252.
- [23] S. Boulfrad, M. Cassidy, E. Djurado, J. T. S. Irvine, G. Jabbour, *Int. J. Hydrogen Energy* **2013**, 38, 9519.
- [24] S. Tao, J. T. S. Irvine, S. M. Plint, *J. Phys. Chem. B* **2006**, 110, 21771.
- [25] A. H. Bork, *Ph.D. Dissertation*, ETH Zurich **2017**.
- [26] J. Mizusaki, H. Tagawa, K. Naraya, T. Sasamoto, *Solid State Ionics* **1991**, 49, 111.
- [27] J. Mizusaki, S. Yamauchi, K. Fueki, A. Ishikawa, *Solid State Ionics* **1984**, 12, 119.
- [28] A. H. Bork, M. Kubicek, M. Struzik, J. L. M. Rupp, *J. Mater. Chem. A* **2015**, 3, 15546.
- [29] E. Povoden-Karadeniz, M. Chen, T. Ivas, A. N. Grundy, L. J. Gauckler, *J. Mater. Res.* **2012**, 27, 1915.
- [30] C. L. Muhich, B. W. Evanko, K. C. Weston, P. Lichty, X. Liang, J. Martinek, C. B. Musgrave, A. W. Weimer, *Science* **2013**, 341, 540.
- [31] M. Tou, R. Michalsky, A. Steinfeld, *Joule* **2017**, 1, 146.
- [32] B. J. Hathaway, R. Bala Chandran, A. C. Gladen, T. R. Chase, J. H. Davidson, *Energy Fuels* **2016**, 30, 6654.
- [33] Y. Hao, C.-K. Yang, S. M. Haile, *Phys. Chem. Chem. Phys.* **2013**, 15, 17084.
- [34] S. Dey, C. N. R. Rao, *ACS Energy Lett.* **2016**, 1, 237.
- [35] I. Al-Shankiti, B. D. Ehrhart, A. W. Weimer, *Sol. Energy* **2017**, 156, 21.
- [36] Q. Jiang, J. Tong, G. Zhou, Z. Jiang, Z. Li, C. Li, *Sol. Energy* **2014**, 103, 425.
- [37] A. H. McDaniel, E. C. Miller, D. Arifin, A. Ambrosini, E. N. Coker, R. O'Hayre, W. C. Chueh, J. Tong, *Energy Environ. Sci.* **2013**, 6, 2424.
- [38] B. D. Ehrhart, C. L. Muhich, I. Al-Shankiti, A. W. Weimer, *Int. J. Hydrogen Energy* **2016**, 41, 19881.
- [39] L. Vegard, *Z. Phys.* **1921**, 5, 17.
- [40] R. D. Shannon, *Acta Crystallogr. A* **1976**, 32, 751.
- [41] V. B. Vert, F. V. Melo, L. Navarrete, J. M. Serra, *Appl. Catal., B* **2012**, 115–116, 346.
- [42] M. N. Iliev, M. V. Abrashev, V. N. Popov, V. G. Hadjiev, *Phys. Rev. B* **2003**, 67, 3.
- [43] M. N. Iliev, A. P. Litvinchuk, V. G. Hadjiev, Y.-Q. Wang, J. Cmaidalka, R.-L. Meng, Y.-Y. Sun, N. Kolev, M. V. Abrashev, *Phys. Rev. B* **2006**, 74, 214301.
- [44] A. Dubroka, J. Humlíček, M. V. Abrashev, Z. V. Popović, F. Sapiña, A. Cantarero, *Phys. Rev. B* **2006**, 73, 1.
- [45] J. Andreasson, J. Holmlund, C. S. Knee, M. Käll, L. Börjesson, S. Naler, J. Bäckström, M. Rübhausen, A. K. Azad, S. G. Eriksson, *Phys. Rev. B* **2007**, 75, 1.
- [46] M. Vračar, A. Kuzmin, R. Merkle, J. Purans, E. A. Kotomin, J. Maier, O. Mathon, *Phys. Rev. B* **2007**, 76, 1.
- [47] C. L. Bull, P. F. McMillan, *J. Solid State Chem.* **2004**, 177, 2323.
- [48] A. G. Souza Filho, J. L. B. Faria, I. Guedes, J. M. Sasaki, P. T. C. Freire, V. N. Freire, J. Mendes Filho, M. M. Xavier, F. A. O. Cabral, J. H. de Araújo, J. A. P. da Costa, *Phys. Rev. B* **2003**, 67, 052405.
- [49] Y. Fujioka, J. Frantti, M. Kakihana, *J. Phys. Chem. B* **2004**, 108, 17012.
- [50] G. Kotnana, S. N. Jammalamadaka, *J. Appl. Phys.* **2015**, 118, 124101.
- [51] I. G. Siny, R. S. Katiyar, A. S. Bhalla, *J. Raman Spectrosc.* **1998**, 29, 385.
- [52] A. Yaremchenko, A. V. Kovalevsky, V. V. Kharton, *Solid State Ionics* **2008**, 179, 2181.
- [53] R. Saravanan, N. Thenmozhi, Y. P. Fu, *Phys. B* **2016**, 493, 25.
- [54] S. P. Jiang, J. P. Zhang, K. Foger, *J. Electrochem. Soc.* **2000**, 147, 3195.
- [55] S. P. Jiang, S. Zhang, Y. D. Zhen, *J. Electrochem. Soc.* **2006**, 153, A127.
- [56] C. L. Muhich, K. C. Weston, D. Arifin, A. H. McDaniel, C. B. Musgrave, A. W. Weimer, *Ind. Eng. Chem. Res.* **2015**, 54, 4113.
- [57] T. Cooper, J. R. Scheffe, M. E. Galvez, R. Jacot, G. Patzke, A. Steinfeld, *Energy Technol.* **2015**, 3, 1130.
- [58] M. Takacs, M. Hoes, M. Caduff, T. Cooper, J. R. Scheffe, A. Steinfeld, *Acta Mater.* **2016**, 103, 700.

- [59] Q. Jiang, Z. Chen, J. Tong, M. Yang, Z. Jiang, C. Li, *Chem. Commun.* **2017**, 53, 1188.
- [60] B. Bulfin, *Phys. Chem. Chem. Phys.* **2019**, 21, 2186.
- [61] D. Marxer, P. Furler, J. Scheffe, H. Geerlings, C. Falter, V. Batteiger, A. Sizmann, A. Steinfeld, *Energy Fuels* **2015**, 29, 3241.
- [62] M. Takacs, J. R. Scheffe, A. Steinfeld, *Phys. Chem. Chem. Phys.* **2015**, 17, 7813.
- [63] T. C. Davenport, M. Kemei, M. J. Ignatowich, S. M. Haile, *Int. J. Hydrogen Energy* **2017**, 42, 16932.
- [64] I. Ikemoto, K. Ishii, S. Kinoshita, H. Kuroda, M. A. Alario Franco, J. M. Thomas, *J. Solid State Chem.* **1976**, 17, 425.
- [65] G. P. Halada, C. R. Clayton, *J. Electrochem. Soc.* **1991**, 138, 2921.
- [66] J. Moulder, W. Stickle, P. Sobol, K. Bomben, in *Handbook of X-Ray Photoelectron Spectroscopy* (Ed: J. Chastain), Perkin-Elmer Corp, Eden Prairie **1992**.
- [67] Q. H. Wu, M. Liu, W. Jaegermann, *Mater. Lett.* **2005**, 59, 1480.
- [68] C. A. Schneider, W. S. Rasband, K. W. Eliceiri, *Nat. Methods* **2012**, 9, 671.